J Mater Sci: Mater Electron

Silver nanoparticulate antenna tracks sintered under carboxylic acid vapors for flexible radio-frequency identification tag application

Justin Courville[1], William Wirth[1], Karl Young[1], and Seonhee Jang[1,*]

[1] Department of Mechanical Engineering, University of Louisiana at Lafayette, Lafayette, LA 70503, USA

Received: 23 June 2022
Accepted: 5 October 2022

ABSTRACT

Sintering of silver (Ag) nanoparticles (NPs) using carboxylic acid vapors was introduced for conductive patterns applicable for flexible radio-frequency identification (RFID) tag application. The printed Ag NP patterns on flexible polyimide sheets were sintered in the atmosphere selected from air, N_2, or N_2-bubbled carboxylic acids. The sintering temperature was chosen from 80, 140, and 200 °C. Microstructures, organic residues, and electrical and mechanical properties of the sintered Ag patterns were compared, depending on sintering atmospheres. The Ag NP patterns sintered in N_2-bubbled formic acid (FA) atmosphere revealed an effective decomposition of organic materials in the patterns, resulting in lower electrical resistance and improved mechanical hardness. The Ag pattern sintered in FA showed relatively low resistances with 0.029–0.039 Ω for all temperatures. Upon folding tests, the Ag NP pattern sintered in FA showed the smallest change in the resistance. The Ag NP pattern sintered in FA at 140 °C had its highest hardness of 3.59 N/mm^2. Sintering conditions in FA at 140 °C for 1.5 min were chosen for the fabrication of flexible RFID tags with two different shapes of squared and spiral antennas. The quality factor (Q-factor) was in the range of 7.775–34.817 and 7.241–78.156, for squared and spiral antennas, respectively.

1 Introduction

Conductive metal pastes or inks play an important role in producing desired conductive layers onto flexible substrates for fabricating various flexible electronics such as flexible or wearable electronic devices, solar cells, identification tags, and smart sensors [1–11]. The conductive electrodes, patterns, and circuits can be formed by either metal sputtering method or printing of metal pastes or inks. The former needs an expensive and complex vacuum system to deposit metal films and the latter enables fast, easy, and cost-effective process. Copper (Cu) and silver (Ag) are the most common conducting materials for metal pastes or inks. Cu is more cost-effective and has high conductivity and less electromigration

Address correspondence to E-mail: seonhee.jang@louisiana.edu

https://doi.org/10.1007/s10854-022-09274-7
Published online: 17 October 2022

effects [12, 13]. However, Cu can be easily oxidized when it is exposed to air, resulting in the insulating Cu oxide layer and reducing the electrical conductivity. In comparison, Ag is the most common conductive ink due to its high conductivity and good oxidation resistance [14–16]. Metal pastes or inks are composed of metal nanoparticles (NPs), organic capping molecules, solvents, and additives. Under appropriate sintering conditions, organic materials in the pastes or inks are removed and metal NP contacts are enhanced to achieve a high electrical conductivity. Researchers have achieved a low temperature sintering of Ag NP pastes and inks to fabricate conductive patterns under atmospheres such as air, nitrogen, or vacuum [17–19].

In this study, diverse sintering atmospheres chosen from carboxylic acids have been adopted to investigate the effect of sintering atmospheres on material properties of conductive patterns using Ag NP inks. Microstructures, organic residues, electrical resistance, and mechanical hardness were observed and compared, depending on sintering conditions. Optimized sintering conditions were employed to fabricate radio-frequency identification (RFID) antenna tags to evaluate the electrical performance and to observe possibility of application for flexible electronics.

2 Experimental details

A printing system was assembled by a single-nozzle pneumatic dispenser (Musashi ML-5000 XII) and a desktop 3D printer. The dispenser comprised a syringe, nozzle, and dispenser controller was suitable for dispensing a small volume of fluid. The dispenser controller had a pneumatic control unit, having an air pulse stabilizing circuit that eliminates fluid volume fluctuation. This resulted in high dispensing accuracy and consistency. An air compressor connected to the dispenser provided the syringe and nozzle with a pressure up to 0.7 MPa. The nozzle size was selected from 0.1 to 0.4 mm. Flexible Kapton polyimide (PI) sheets with a thickness of 0.1 mm were used as substrates for printing. The Ag NP ink with a model of PSI-211 was purchased from NovaCentrix and its formulation properties included: Ag solids content of 42 ± 2 wt%, density of 1.6 g/ml, viscosity of 3500–6000 cP at 10 s^{-1}, and acidity of 5.80 ± 0.05 pH. Overall size of Ag NPs was measured from the transmission electron microscope images. About 56% of particles had the size below 10 nm and the average particle size was approximately 18 nm. Line patterns with a width of 1 mm and a length of 20 mm were designed in the format of G-code and loaded in the 3D printer. After the Ag NP ink was filled in the syringe of the dispenser, the pressure was injected into the syringe and nozzle from the air compressor and the ink was ejected as droplets from the nozzle. Then, Ag NP patterns were printed on the PI substrate according to the pattern images. The printed patterns were then dried in air before sintering.

The printed and dried Ag patterns were placed on the hot plate covered with a stainless-steel box for sintering process. The box was tightly sealed on top of the hot plate and connected with a quarter-inch tube for supply of sintering gas. Sintering gas was selected from air, N_2, or N_2-bubbled carboxylic acids. Carboxylic acids included: monocarboxylic acids such as acetic acid (AA, $C_2H_4O_2$), butyric acid (BA, $C_4H_8O_2$), formic acid (FA, CH_2O_2), and propionic acid (PA, $C_3H_6O_2$), dicarboxylic acid such as oxalic acid (OA, $C_2H_2O_4$), and tricarboxylic acid such as citric acid (CA, $C_6H_8O_7$). Purity of N_2 gas was 99.8%. All chemical reagents with ACS 96+% were purchased from Fisher Scientific. No process gas was provided in the box for sintering in air. For sintering in N_2, N_2 gas was introduced to the box through the quarter-inch tube from the N_2 gas cylinder with a pressure of 15 psi controlled by a gas regulator. For sintering in N_2-bubbled carboxylic acids, a glass jar having both inlet and outlet was prepared. After filling with each carboxylic acid, the inlet and outlet were connected to the N_2 gas cylinder and the box through the quarter-inch tubes, respectively. N_2 gas flowed into the jar though the outlet generated bubbles in the acid and these N_2-bubbled carboxylic acid vapors were introduced into the box through the inlet. When the dried Ag NP patterns were placed at the center of the hot plate enclosed by the box, the hot plate was heated up to reach the set temperature with a ramping rate of 16.7 °C/min and the sintering gas was supplied into the box. Sintering temperature was set below 200 °C to avoid the degradation of the PI substrate. Sintering temperatures were chosen among 80, 140, and 200 °C and a duration time for sintering was 1.5 min. Once the sintering process was completed, the sintered Ag patterns were released after the box was cool down to room temperature.

Microstructures of sintered Ag NP patterns were examined using scanning electron microscopy (SEM, S-4500 Type II, Hitachi) with the secondary electron image resolution of 1.5 nm at 15 kVA and the magnification up to ×50,000. Crystallinity of the patterns was observed using X-ray diffractometry (XRD, Miniflex600, Rigaku) with CuKα (1.5406 Å) radiation. Electrical resistance of Ag NP patterns was measured using a four-point probe (Ossila). Surface morphology and root mean square (RMS) roughness of Ag NP patterns were observed using atomic force microscopy (AFM, Dimension 3100, Veeco). Optical image of the patterns was examined using optical microscopy (HAL 100, Axiotech). Chemical composition of organic residues remained in sintered Ag NP patterns was measured using Fourier transform infrared (FTIR) spectroscopy (FTIR-4700, Jasco). Microindentation hardness tester (Micromet 5103, Buehler) with a Vickers indenter was conducted to measure the Vickers hardness.

To evaluate the electrical performance of sintered Ag NP patterns, RFID antenna tags were fabricated and characterized. Electrical characteristics of the RFID antenna tag were determined in a 13.56 MHz band using a network analyzer (N5234A PNA-L Network Analyzer, Keysight Technologies). Figure 1a and b show schematic diagrams of squared and spiral antennas, respectively. Dimensions with inner diameter (d_{in}), outer diameter (d_{out}), inner radius (r_{in}), and outer radius (r_{out}) are indicated for each diagram. Figure 1c and d present photos of sintered Ag NP patterns on flexible PI substrate for squared and spiral antennas, respectively.

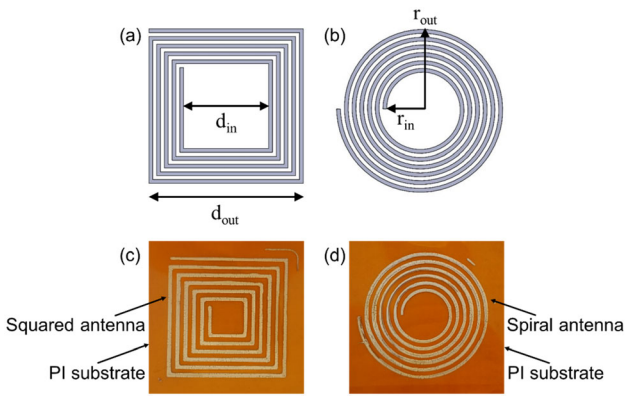

Fig. 1 Schematic diagram of **a** squared and **b** spiral antennas and photos of sintered Ag NP patterns on flexible PI substrate for **c** squared and **d** spiral antennas

Figure 2 shows the schematic diagram for setup with the network analyzer to measure the return loss (S_{11}) of the RFID antenna tag. An RFID transponder was chosen from one of the I2C chips, M24LR04E-R (13.56 MHz) purchased from STMicroelectronics. Two wires were connected to the antenna terminals with the I2C chip to create an RFID receiver. The receiver was then linked to the network analyzer to measure the return loss (S_{11}). The network analyzer was connected to the ground pin of the I2C and one of the antenna terminals. The chip had an internal tuning capacitance (C_1) of 27.5 pF. An additional tuning capacitor (C_2) was connected in parallel with the C_1 depending on antenna types.

3 Results and discussion

3.1 Electrical resistance and microstructure

Figure 3 presents the resistances of the Ag NP patterns sintered in various sintering atmospheres and temperatures. The sintering atmosphere was chosen from air, N_2, and N_2-bubbled carboxylic acids including AA, BA, FA, PA, OA, and CA. The sintering temperature was selected from 80, 140, and 200 °C, and sintering time was 1.5 min. The resistances strongly depended on the sintering temperature and atmosphere. When the Ag NP patterns were sintered at 80 °C, average resistances were measured above 20 Ω for N_2, AA, BA, CA, and OA, and no resistance was measured for air while the lowest resistance of 0.039 Ω was obtained for FA, followed by 9.636 Ω for PA. As the sintering temperature increased to 140 and 200 °C, the resistances drastically decreased below 1 and 0.1 Ω for all sintering

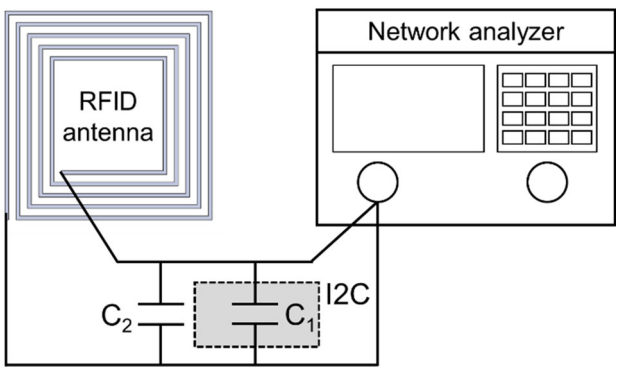

Fig. 2 Schematic diagram for setup with the network analyzer to measure the return loss (S_{11}) of the RFID antenna tag

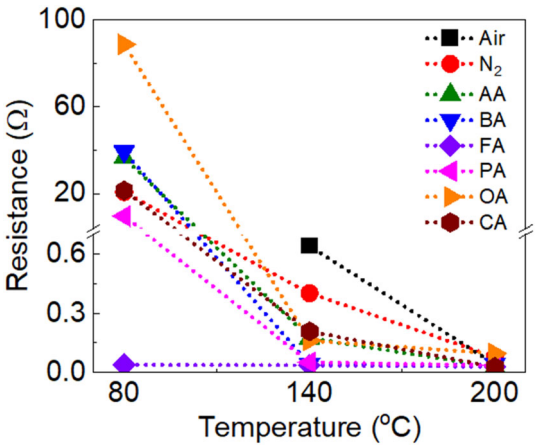

Fig. 3 Resistances of the Ag NP patterns sintered in air, N_2, and N_2-bubbled carboxylic acids of AA, BA, FA, PA, OA, and CA for 1.5 min at sintering temperatures of 80, 140, and 200 °C

atmospheres, respectively. Interestingly, the Ag pattern sintered in FA maintained relatively low resistances with 0.039, 0.036, and 0.029 Ω for all temperatures of 80, 140, and 200 °C, respectively while the Ag patterns sintered in other atmospheres showed higher resistances at 80 °C.

Figure 4a–h represent the SEM microstructures of the Ag NP patterns sintered in air, N_2, and N_2-bubbled various carboxylic acids including AA, BA, FA, PA, OA, and CA, respectively. Sintering temperature and time were 140 °C and 1.5 min, respectively. A metallic NP ink is generally composed of metal NPs dispersed in a carrier solvent. The solvent mainly functions as a carrier without degrading the metal NPs. Organic capping molecules as dispersing agents enclose the metal NPs to prevent agglomeration or oxidation of them as well as to control the shape and size of the metal NPs during a synthesis of them. Additives are also included with a small amount below 5% by weight to determine the properties of the ink such as tension, rheology, wettability, and dispersion stability. Although information of all organic materials in the ink was not disclosed, it is generally accepted that organic materials derived from the ingredients of the ink should be eliminated by the sintering process to enhance electrical conductivity. The removal of the capping molecules during the sintering process also promotes the contact of the metal NPs, causing further networking and coalescence of the NPs and densification of the NP film. For sintering in air or N_2, some large grains were observed but particles were remained and dispersed. The Ag NP patterns sintered in N_2-bubbled carboxylic acids showed some distinct characteristics. When the particles make contact each other, a neck between them occur instantly. The neck generally grows by mass transport and diffusion and the grains and grain boundaries are formed. Along with the formation of grains and grain boundaries, pores reach their equilibrium shapes. Pores give channels along the grain edges and their shrinkage due to grain growth contributes to the densification of the film. It was expected that grain growth, pore

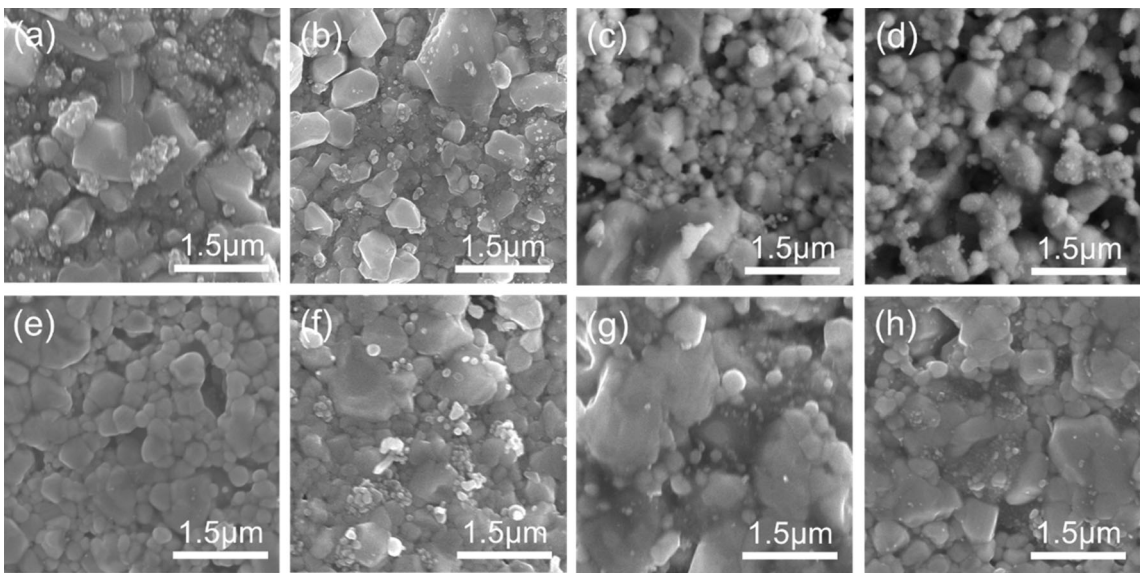

Fig. 4 SEM surface images of the Ag NP patterns sintered in **a** air, **b** N_2, and N_2-bubbled carboxylic acids of **c** AA, **d** BA, **e** FA, **f** PA, **g** OA, and **h** CA at 140 °C for 1.5 min

distribution, unsintered particles, and organic residues could affect the properties of the Ag NP patterns. It is likely that pore distribution was observed for all carboxylic acids. Unsintered particles were scattered in the microstructure of the patterns sintered in all carboxylic acids except for FA although larger grains were presented for sintering in PA, OA, and CA. For sintering in FA, both coalescence and grain growth were observed.

Figure 5a–f show the SEM microstructures of the Ag NP patterns sintered in CA at 80, 140, and 200 °C and in FA at 80, 140, and 200 °C, respectively. Sintering time was 1.5 min. The resistances were 21.450, 0.208, and 0.028 Ω for sintering in CA at 80, 140, and 200 °C, respectively, and 0.039, 0.036, and 0.029 Ω for sintering in FA at 80, 140, and 200 °C, respectively. For sintering in CA at 80 °C, it is likely that most particles were remained without participating in any coalescence and grain growth. In comparison, network structures and agglomeration were found for sintering in FA at 80 °C. This difference in their microstructures at 80 °C resulted in the big difference in their resistances. It is probable that there could be organic residues remained in the microstructure when unsintered particles were still observed. These organic residues could be one of the factors to having higher electrical resistances. It could be explained that higher resistance for sintering in CA at 140 °C was due to unsintered particles, compared with that for sintering in FA at 140 °C. At 200 °C, both microstructures for sintering in CA and FA were very similar with coalescence and grain growth and this resulted in almost the same resistance.

During sintering process, an effective removal of organic capping molecules is mostly important in order the particles to make contact each other. After organic capping molecules are removed, the Ag NPs contact each other and an instantaneous neck formation occurs between the NPs, followed by the neck growths through mass transport and diffusion and grain boundaries formation and grain growth. It is likely that formic acid played an important role in eliminating capping molecules effectively and acted as a facilitator to accelerate the contact and aggregation of NPs during sintering process. It is probable that formic acid functioned as an etchant to decompose organic compounds due to their acidity and reaction with organic materials. It should be noted that the reaction between formic acid vapors and organic materials couldn't be identified because the composition of the Ag NP ink was not disclosed by the manufacturer. At the low sintering temperature of 80 °C, microstructures demonstrated that formic acid was more effective than citric acid. More agglomeration was found for sintering in FA and some scattered unsintered particles were observed for sintering in CA. More agglomeration in the microstructure for sintering in FA led to lower electrical resistance. As a result, for the low temperature sintering process, formic acid was more effective than

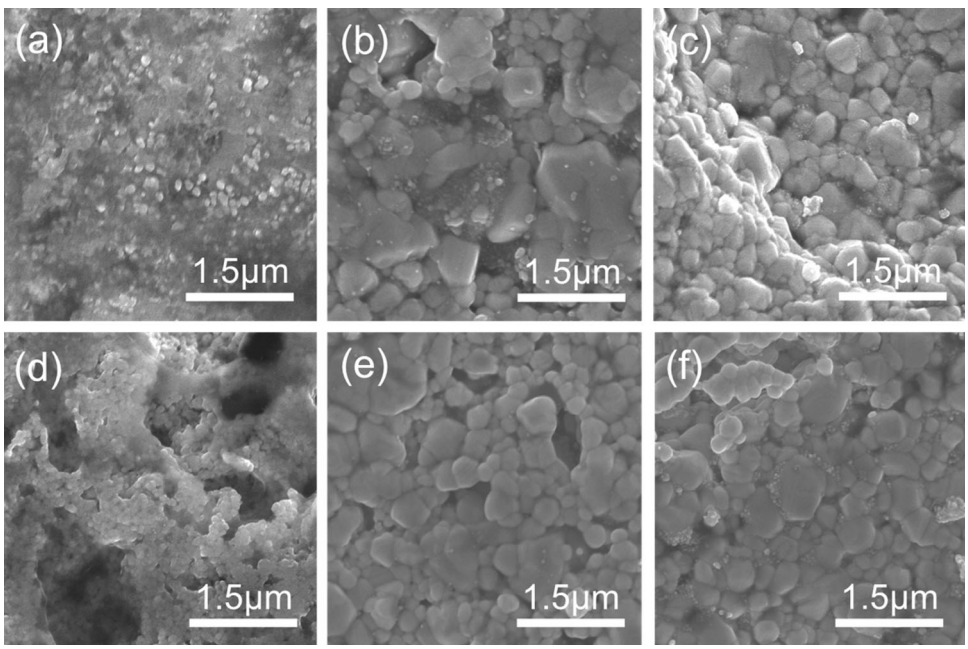

Fig. 5 SEM surface images of the Ag NP patterns sintered in CA at **a** 80, **b** 140, and **c** 200 °C and FA at **d** 80, **e** 140, and **f** 200 °C for 1.5 min

citric acid. When the sintering temperature increased to 140 and 200 °C, the decomposition of the capping molecules became easier and the contact between the NPs, neck formation, and grain growth were more progressed for both FA and CA cases. There was little difference in microstructures for both cases at 200 °C, consistent with the electrical resistance results. At the high sintering temperature such as 200 °C, a dominant factor to determine the microstructure and electrical resistance was the temperature rather than the atmosphere.

3.2 Surface morphology and optical surface imagery

Figure 6a–h show the AFM surface morphologies of the Ag NP patterns sintered in air, N_2, and N_2-bubbled carboxylic acids including AA, BA, FA, PA, OA, and CA, respectively. Sintering temperature and time were 140 °C and 1.5 min, respectively. As seen in the SEM microstructures, the grains recognized by grain boundaries as well as unsintered particles were observed. The RMS roughness values of the Ag NP patterns sintered in air, N_2, and N_2-bubbled carboxylic acids including AA, BA, FA, PA, OA, and CA were calculated as 71.6, 94.2, 60.7, 89.3, 74.8, 72.4, 98.8, and 63.6 nm, respectively. The RMS average was obtained by measuring the average height deviations of the mean line. The RMS roughness was calculated by measuring the height of a surface's microscopic peaks and valleys, squaring those measurements, determining the average of the squares, and finding the square root of that number. The lowest RMS value of 60.7 nm was obtained for sintering in AA. The morphology of the Ag pattern sintered in AA showed relatively smaller grains along with unsintered Ag NPs and this could cause the lowest RMS value. The morphology of the Ag pattern sintered in OA showed larger grains although some unsintered Ag NPs were observed. The RMS roughness values was 98.8 nm for OA. The pattern sintered in FA showed somewhat low RMS value of 74.8 nm with no indication of unsintered NPs. It is likely that the grain growth of NPs is related to the surface roughness.

Figure 7a–h represent the optical surface images of the Ag NP patterns sintered in air, N_2, and N_2-bubbled carboxylic acids including AA, BA, FA, PA, OA, and CA, respectively, with a magnification of 20 times. Sintering temperature and time were 140 °C and 1.5 min, respectively. No cracks propagated to the bottom of the patterns were observed for all cases. Overall images showed smooth and uniform surface with no physical defects. The grooves on the surface were found in the patterns sintered in air and did not penetrate down to the substrate. Small pits or craters were observed in the patterns sintered in AA, BA, PA, OA, and CA. The pits or craters were much smaller than the grooves from the pattern sintered in air.

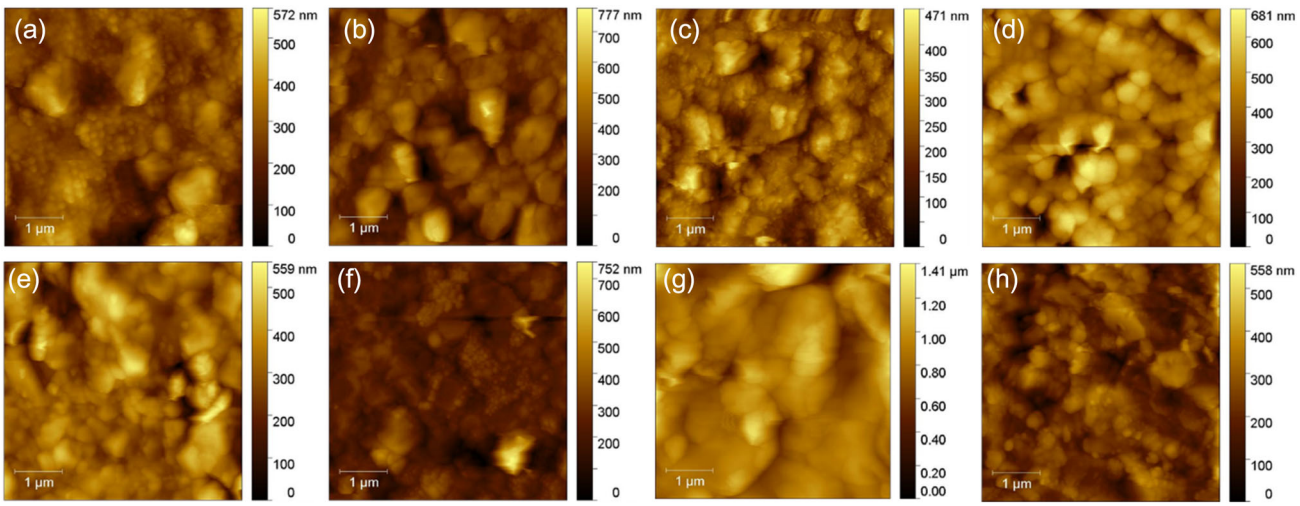

Fig. 6 AFM surface morphologies of the Ag NP patterns sintered in **a** air, **b** N_2, and N_2-bubbled carboxylic acids of **c** AA, **d** BA, **e** FA, **f** PA, **g** OA, and **h** CA at 140 °C for 1.5 min

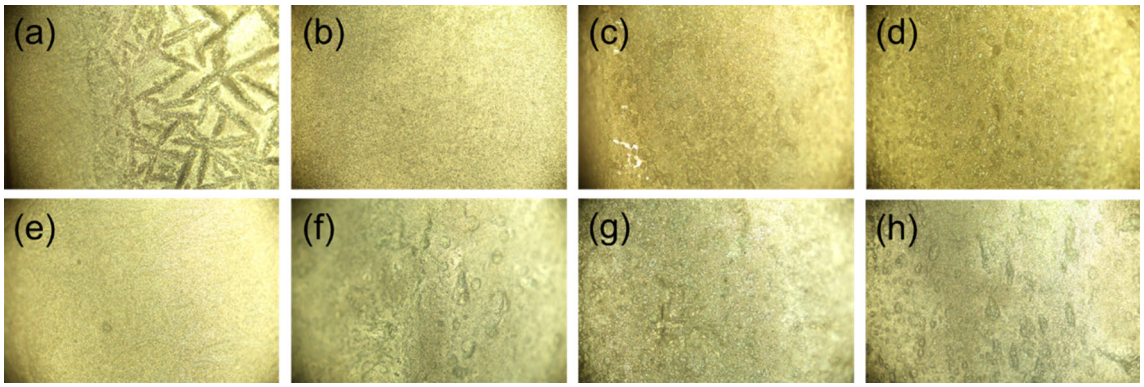

Fig. 7 Optical images taken at ×20 magnification of the Ag NP patterns sintered in **a** air, **b** N_2, and N_2-bubbled carboxylic acids of **c** AA, **d** BA, **e** FA, **f** PA, **g** OA, and **h** CA at 140 °C for 1.5 min

3.3 XRD analysis

Figure 8 shows the XRD patterns of the Ag NP patterns sintered in air, N_2, and N_2-bubbled carboxylic acids including AA, BA, FA, PA, OA, and CA. Sintering temperature and time were 140 °C and 1.5 min, respectively. For all samples, five diffraction peaks corresponded to the diffraction of planes (111), (200), (220), (311), and (222) of the face-centered cubic (FCC) structure of Ag, assigned to approximately 38.2°, 44.4°, 64.5°, 77.5°, and 81.6°, respectively. These planes with their corresponding diffraction angle (2θ) were confirmed by the standard JCPDS Card No. 04-0783. The highest peak intensity for the plane (111) was obtained among five peaks for all sintering atmospheres. The grain size for each sintering atmosphere was calculated using the Scherrer equation given by $D = \frac{K\lambda}{\beta\cos\theta}$, where D is the average crystallite size, λ is the X-ray wavelength, β is the width of the X-ray peak on the 2θ axis, normally measured as full width at half maximum (FWHM), θ is the diffracted Bragg angle, and K is the so-called Scherrer constant [20]. K depends on the crystallite shape and the size distribution, indices of the diffraction line, and the actual definition used for β whether FWHM or integral breadth [21]. K can have values anywhere from 0.62 to 2.08. In this paper, K = 0.90 was used. The overall average grain sizes were in the range of 18–21 nm. The largest and smallest grain sizes were calculated for sintering in OA and CA, respectively.

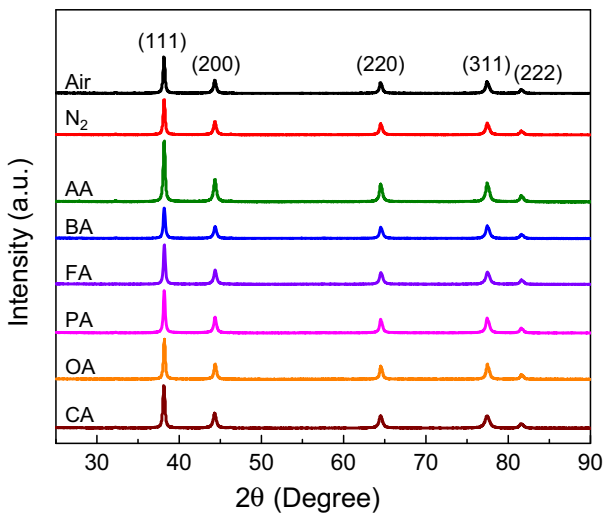

Fig. 8 XRD patterns of the Ag NP patterns sintered in air, N_2, and N_2-bubbled carboxylic acids of AA, BA, FA, PA, OA, and CA at 140 °C for 1.5 min

For studying the electrical resistivity behavior of polycrystalline metal films, contributions of surfaces and grain boundaries are important [22–26]. Metal films in nanometer dimensions show higher electrical resistivity due to additional scattering centers for the conduction electrons, mainly from surfaces and grain boundaries. When the film surface is smooth enough, the resistivity is dominated by the effect of grain boundaries. As the surface roughness becomes larger, a substantial increase in the resistivity is observed. It was also reported that the films exhibit a stronger grain boundaries effect when grains are smaller [22]. From the analyses of the electrical resistance, surface roughness, and grain size, comparing results between two cases of FA and OA, it was found that large grain size (21 nm) and high RMS (98.8 nm) for OA resulted in a high resistance (0.162 Ω) and relatively small grain size (20 nm) and low RMS (74.8 nm) for FA resulted in a low resistance (0.036 Ω). Because there was little difference in grain sizes, it is likely that the surface roughness contributed dominantly to the

resistance. However, for sintering in AA and CA, both RMS (60.7 and 63.6 nm) were small compared to those for the rest of sintering atmospheres, but the resistance was high with their respective values of 0.174 and 0.208 Ω. Therefore, the effect of surface roughness and grain size on the electrical resistance can't be explained by citing the references [22–26]. It is probable that other factors affecting the resistance can be considered. The organic residues could determine the electrical resistance. Organic residues remained the patterns would cause a high electrical resistance. More agglomeration and grain growth would be an indication of less organic residues because they generally occur after contacting particles when organic residues (mainly capping molecules) are removed. Unsintered particles scattered in the pattern could lead to a high resistance because joining and networking between particles for electrical paths are not fully accomplished. Pores in the microstructure would affect the roughness as well as the electrical resistance. Dense microstructure with less pores would result in a low resistance.

3.4 FTIR analysis

Figure 9a and b present the FTIR spectra of Ag NP ink and the Ag NP patterns sintered in air, N_2, and N_2-bubbled carboxylic acids including AA, BA, FA, PA, OA, and CA, respectively. Sintering temperature and time were 140 °C and 1.5 min, respectively. The Ag NP ink contained organic materials including a carrier solvent, capping molecules, and additives. This reflected various chemical bonds in the spectra including O–H stretching, C–H stretching, C–H stretching, O–H bending, and C–H bending modes, assigned to 3400–3200, 3000–2800, 1700–1600, 1400–1300, and 850–750 cm^{-1}, respectively. Because the Ag NP ink was an aqueous based ink, two O–H chemical bonds were detected from the spectra. Ideally, the sintered Ag NP patterns should not include any organic residues after the decomposition of all organic materials. However, insufficient sintering conditions could result in organic residues left in the patterns because some organic materials may not be completely decomposed. The FTIR spectra are useful to identify the organic residues. All Ag NP patterns showed C–H stretching, C–O stretching, C–O stretching, and C–H bending modes, corresponding to 3000–2800, 1300–1200, 1100–1000, and 850–750 cm^{-1}, respectively. It is probable that these chemical bonds were induced from undecomposed capping molecules and additives. The O–H stretching and bending modes from the ink disappeared after sintering. Although there was not considerable change in the peak intensity of C–H stretching at 3000–2800 cm^{-1} for all cases, depressed C–O stretching and C–H bending modes at 1300–1250 and 1100–1050 cm^{-1} were observed for air and N_2 cases. The resistances of the Ag patterns sintered in air or N_2 showed almost one order higher than that in FA but there was little change in the FTIR spectra. Thus, other factors should be considered to determine the relationship between the electrical resistance and organic residues.

3.5 Mechanical folding test

Figure 10 presents the resistance ratio (R/R_0) of the Ag NP patterns sintered in various sintering atmospheres at 140 °C for 1.5 min after folding tests with folding cycles between 10 and 50. The R_0 and R were resistances before and after folding test, respectively.

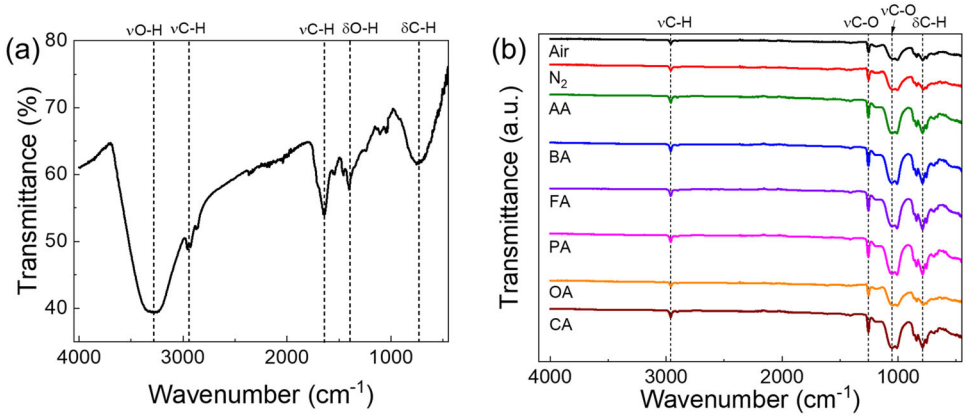

Fig. 9 FTIR spectra of **a** Ag NP ink and **b** Ag NP patterns sintered in air, N_2, and N_2-bubbled carboxylic acids of AA, BA, FA, PA, OA, and CA at 140 °C for 1.5 min

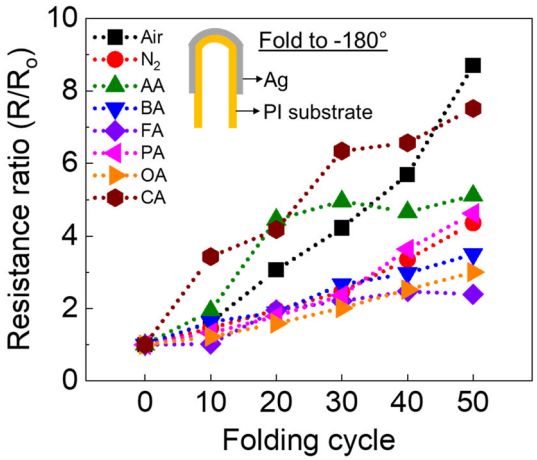

Fig. 10 Changes in resistance (R/R_0) of the Ag NP patterns sintered in various sintering atmospheres at 140 °C for 1.5 min after folding tests with folding cycles between 10 and 50

An inlet is a schematic diagram of folding test. The PI substrate with sintered Ag NP patterns on it was loaded in the folding tester, folded to − 180°, and released back to 0°. The resistance values were recorded every 10 folding cycles. Overall, the resistance increased as the number of folding cycles increased. The largest change in the resistance after 50 folding cycles was observed for the Ag NP pattern sintered in air with 8.70 for $\frac{R}{R_0}$. In comparison, the Ag NP pattern sintered in FA showed a gradual increase in the resistance as the number of folding cycles increased and the smallest change in the resistance with 2.39 for $\frac{R}{R_0}$. Thus, the most reliable mechanical stability was obtained for the Ag NP pattern sintered in FA.

Figure 11a–h shows the optical surface images of the Ag NP patterns sintered in air, N_2, and N_2-bubbled carboxylic acids including AA, BA, FA, PA, OA, and CA, respectively, with a magnification of 20 times, after folding tests with 50 cycles. Sintering temperature and time were 140 °C and 1.5 min, respectively. It was observed that cracks had formed across the surface of the patterns. The Ag patterns sintered in air and CA experienced a drastic change in resistance and developed larger cracks. These cracks separated the patterns into sections. The cracks in the pattern sintered in air followed the grooves that were present after sintering, giving the cracks a chance to form in the weaker section of the patterns. These cracks were larger than others found in the different atmospheric conditions. The Ag pattern sintered in CA had cracks generating in the longitudinal direction of the conductive lines. Most cracks were primarily located in the center of the conductive lines, leaving the edges free of cracks. Fewer cracks were found in the Ag patterns sintered in FA, resulting in a small change in resistance after folding test. It suggests that the cracks were just present on the surface of the patterns and did not spread down to the substrate. Some cracks found in the Ag patterns sintered in N_2 and AA expanded across the width of the line and caused increased resistance. When performing the folding tests on the Ag patterns sintered in AA, BA, PA, and OA, the sections of the patterns were missing. Cracks were generated early in the folding cycle. As the folding cycle continued, the cracks developed into larger cracks, and eventually, a section broke off or rubbed away, making a hole in the Ag patterns. As sections started to break off, the cracks formed on the edges of the hole, causing the size of the hole to increase and the increase in the resistance as the folding cycles

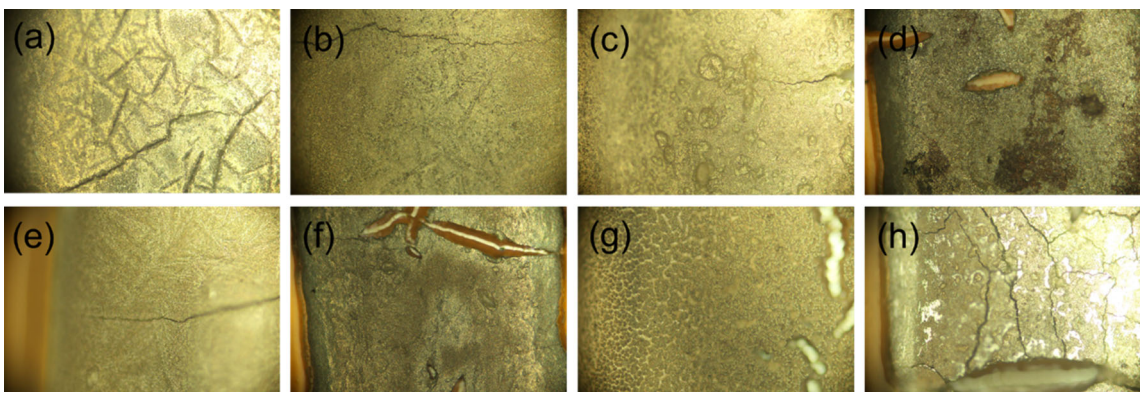

Fig. 11 Optical images taken at ×20 magnification of the Ag NP patterns sintered in **a** air, **b** N_2, and N_2-bubbled carboxylic acids of **c** AA, **d** BA, **e** FA, **f** PA, **g** OA, and **h** CA at 140 °C for 1.5 min after folding tests with 50 cycles

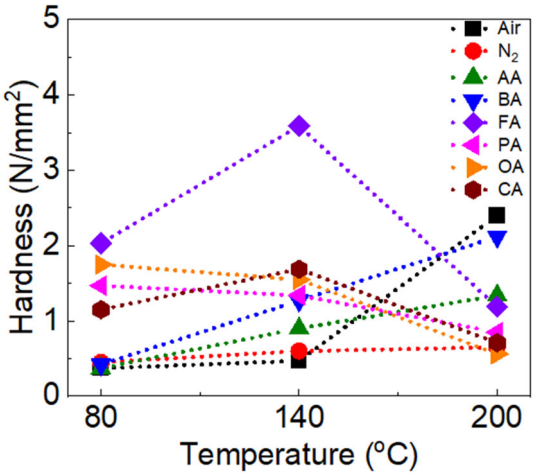

Fig. 12 Vickers hardness of Ag NP patterns sintered in air, N_2, and N_2-bubbled carboxylic acids of AA, BA, FA, PA, OA, and CA for 1.5 min at sintering temperatures of 80, 140, and 200 °C

continued. It is likely that the pits observed in the sintered patterns caused to generate cracks in small areas as sections broke off of the patterns during the folding process.

3.6 Vickers hardness

Figure 12 represents average Vickers hardness (HV) values of sintered Ag NP patterns under various sintering temperatures and atmospheres. Sintering time was 1.5 min for all cases. The HV values are found using the equation, $HV = k\frac{F}{S}$, where HV is the Vickers hardness, k is constant ($k = 1/g_n \approx 0.102$, g_n is the standard acceleration due to gravity), F is the test force (N), and S is the surface area of the indentation (mm^2) found by applying the force to a sample using a quadrangular pyramid diamond indenter. The hardness values were measured in the range of 0.37–2.03, 0.47–3.59, and 0.56–2.12 N/mm^2 for 80, 140, and 200 °C, respectively. As the sintering temperature increased from 80 to 200 °C, the hardness values of the Ag NP patterns sintered in air, N_2, AA, and BA increased while those sintered in PA or OA decreased. In comparison, the Ag NP patterns sintered in FA and CA showed their highest hardness at 140 °C. Among all sintering conditions, the Ag NP pattern sintered in FA at 140 °C had the highest hardness of 3.59 N/mm^2. The Ag NP patterns sintered in FA at 140 °C showed the best performance in terms of electrical and mechanical properties: the electrical resistance with a relatively low value of 0.036 Ω, a small change in the resistance with R/R_0 of 2.39 after folding test with 50 cycles, and the highest hardness of 3.59 N/mm^2. For sintering in FA, when the temperature increased from 80 to 140 °C, the hardness increased from 2.03 to 3.59 N/mm^2. When the temperature increased further to 200 °C, the hardness decreased to 1.19 N/mm^2. Because the Ag NP pattern sintered in FA at 140 °C showed the highest hardness, it had a strong resistance to mechanical stress. Thus, the smallest change in electrical resistance was obtained after folding tests up to 50 cycles. It was known that formic acid vapor can be used as a reducing agent due to its reactivity from the –CHO group. It is possible that the –CHO group would react with organic capping molecules and lead to the removal of the capping molecules. As shown in Fig. 12, the hardness decreased when the sintering temperature increased from 140 to 200 °C. It was reported that formic acid could decompose into H_2 and CO_2 when the atmosphere temperature increases more than 167 °C [27]. At the sintering temperature of 200 °C, the –CHO groups could still be effective for sintering however some formic acid could be decomposed, producing H_2 and CO_2. It is unlikely that those decomposed gases contributed to the reaction with the capping molecules. Instead, it is possible that carbon dioxides were deposited on the pattern, forming another type of organic residues and leading to less mechanical strength. If they did not penetrate deep into the thick pattern, it is unlikely that they affected the electrical resistance.

Figure 13 shows the Vickers hardness and resistance of the Ag NP patterns as a function of average grain size ($d^{-1/2}$) calculated from the XRD patterns for various sintering atmospheres at 140 °C for

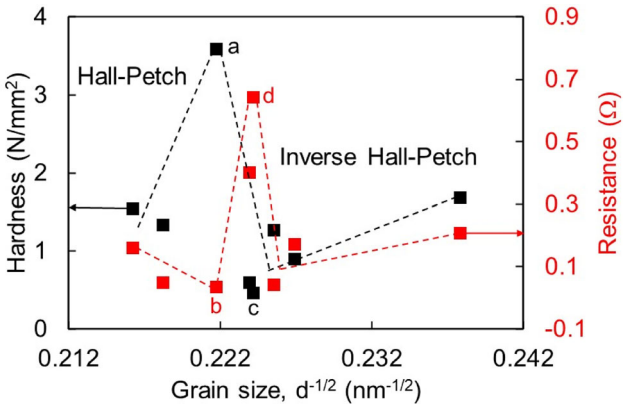

Fig. 13 Vickers hardness and resistance of the Ag NP patterns sintered in various sintering atmospheres at 140 °C for 1.5 min as a function of grain size

Table 1 Antenna types designed with two different shapes of squared and spiral patterns with different dimensions

Antenna	Number of turns	d_{in} (mm)	d_{out} (mm)	r_{in} (mm)	r_{out} (mm)	Line width (mm)	Line spacing (mm)	C_2 (pF)	Equivalent inductance (μH)
SQ1	6	18	40	–	–	1	1	40	1.51
SQ2	5	22	40	–	–	1	1	55	1.27
SQ3	6	13	35	–	–	1	1	70	1.12
SP1	7	–	–	7.5	21.5	1	1	30	1.50
SP2	6	–	–	9.5	21.5	1	1	50	1.33
SP3	6	–	–	7.5	19.5	1	1	70	1.08

1.5 min. The Hall–Petch relationship has been described that the yield stress σ and hence the hardness scales with the inverse square root of grain size, d, in polycrystalline materials and is given by the following equation [28, 29]:

$$\sigma = \sigma_0 + kd^{-1/2}$$

where k is a measure of the local stress needed to initiate plastic flow at a grain boundary and σ_0 is the resistance to dislocation motion in the grain interior [30]. According to the Hall–Petch relationship, the strength of materials can be accomplished by reducing grain size. The strength of materials increases as the grain size decreases to approximately 20–30 nm where the highest strength can be obtained and starts to soften with decreasing grain size below 20 nm. As the grain size decreased, the hardness increased until the $d^{-1/2}$ reached to 0.222 $nm^{-1/2}$ and then decreased. The transition from the Hall–Petch to the inverse Hall–Petch occurred at 0.222 $nm^{-1/2}$ for $d^{-1/2}$ where the highest hardness was found as 3.59 N/mm^2. The sintering atmospheres of OA and PA occupied the Hall–Petch region while those of N_2, air, BA, AA, and CA the inverse Hall–Petch region. The transition occurred for the sintering atmosphere of FA. On the other hand, the resistance decreased as the grain size decreased in the Hall–Petch region. The lowest resistance was obtained at the transition with 0.222 $nm^{-1/2}$ for $d^{-1/2}$. After the transition, the resistance showed an increase at first but a decrease. The highest hardness of 3.59 N/mm^2 (point a) and lowest resistance of 0.036 Ω (point b) were obtained at 0.222 $nm^{-1/2}$ for $d^{-1/2}$, corresponding to the sintering atmosphere of FA and the lowest hardness of 0.47 N/mm^2 (point c) and highest resistance of 0.643 Ω (point d) at 0.224 $nm^{-1/2}$ for $d^{-1/2}$, corresponding to the sintering atmosphere of air.

3.7 Characterization of RFID antenna tag

The antenna patterns were formed by sintering of printed Ag NP ink on the PI substrate in N_2-bubbled FA at 140 °C for 1.5 min. The antenna was designed with two different shapes of squared and spiral patterns with different dimensions as shown in Table 1. Three square antennas (SQ1, SQ2, and SQ3) were designed with outer diameter (d_{out}) of 35 or 40 mm, inner diameter (d_{in}) of 13, 18, or 22 mm, line width of 1 mm, line spacing of 1 mm, and number of turns of 5 or 6. Three spiral antennas (SP1, SP2, and SP3) were designed with outer radius (r_{out}) of 19.5 or 22.5 mm, inner radius (r_{in}) of 7.5 or 9.5 mm, line width of 1 mm, line spacing of 1 mm, and number of turns of 6 or 7. In the design of a 13.56 MHz antenna, the main parameter is the equivalent inductance (L_{ant}). The inductance of squared antennas is calculated by [31, 32]

$$L_{ant} = K1 \times \mu_0 \times N^2 \times \frac{d}{1 + K2 \cdot p}$$

where d is the average diameter given by $\frac{d_{out}+d_{in}}{2}$, p is given by $\frac{d_{out}-d_{in}}{d_{out}+d_{in}}$, and $K1$ and $K2$ depend on the layout and are 2.34 and 2.75, respectively, for a squared antenna.

The inductance of spiral antennas is calculated by [31, 32]

$$L_{ant} = 31.33 \times \mu_0 \times N^2 \times \frac{a^2}{8a + 11c}$$

where a is the average radius given by $\frac{r_{out}+r_{in}}{2}$, c is given by $r_{out} - r_{in}$, and μ_0 is $4\pi \times 10^{-7}$ H/m.

Since large inductance may cause a small capacitance of the tuning capacitor, each antenna was designed to have the equivalent inductance of 1–2 μH by connecting the tuning capacitor (C_2) in parallel with C_1 as shown in Fig. 2 [33].

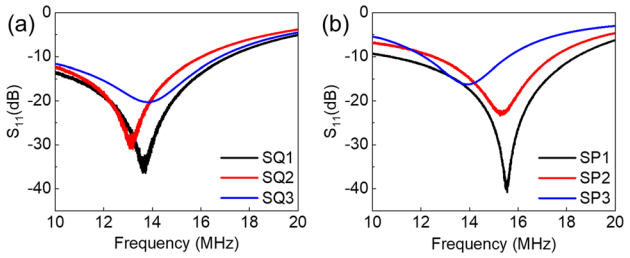

Fig. 14 Return loss (S_{11}) of **a** squared and **b** spiral antenna tags

Figure 14a and b shows return loss (S_{11}) of squared and spiral antenna tags, respectively. Table 2 shows resonance frequency (f_0), return loss (S_{11}) at f_0, full band width at 3 dB above the minimum S_{11} at f_0 (f_{BW}), and quality factor (Q-factor) for all squared and spiral antenna tags. The effective working range of the antenna in frequency was in the range of 10–20 MHz. For squared antennas, the resonance occurred at 13.193–13.832 MHz, and the maximum S_{11} values at the resonance frequency were in the range between − 36.451 and − 20.295 dB. For spiral antennas, the resonance occurred at 13.903–15.553 MHz, and the maximum S_{11} values at the resonance frequency were in the range between − 40.791 and − 16.258 dB. The Q-factor defines as a ratio between resonant circuit stored energy and the resonance band. The Q-factor is generally calculated by $Q = \frac{f_0}{f_{BW}}$, where f_{BW} is the full band width at 3 dB above the minimum S_{11} at the resonance frequency, f_0 [34–38]. A high Q-factor should be obtained to improve the read performance of RFID tags. The Q-factors were in the range of 7.775–34.817 and 7.241–78.156, for squared and spiral antennas, respectively. The Q-factors showed higher values as higher equivalent inductance was applied for each squared and spiral antenna. It has been reported that the Q-factors with 5 to 20 are preferred for RFID antenna tags fabricated in the 13.56 MHz band [39]. Thus, three antennas of SQ3, SP2, and SP3 could be considered for fabrication of desirable RFID antenna tags in the 13.56 MHz band. The Q-factor is generally affected by parameters such as the number of turns, the length, of the antenna, the spacing between turns, and the thickness of antenna patterns.

4 Conclusion

Sintering of Ag NPs was performed using various sintering atmospheres including carboxylic acids for conductive antenna patterns applicable for flexible RFID tag application. The microstructure and organic residues of sintered Ag NP patterns were strongly affected by atmosphere and temperature and resulted in changes in electrical resistance and hardness. Among carboxylic acids, sintering in FA was most effective to remove organic materials and enhance the particles agglomeration and grain growth, resulting in low electrical resistance and high Vickers hardness. The Ag NP pattern sintered in FA at 140 °C for 1.5 min had its lowest resistance with 0.036 Ω and highest hardness of 3.59 N/mm^2. Upon folding tests up to 50 cycles, the Ag NP pattern sintered in FA showed the smallest change in the resistance and less cracks developed on the surface. The Ag pattern sintered in FA at 140 °C for 1.5 min was used for the fabrication of flexible RFID antenna tag with two different shapes of squared and spiral antennas. The resonance frequency and return loss (S_{11}) were measured and the Q-factors were obtained in the range of 7.775–34.817 and 7.241–78.156, for squared and spiral antennas, respectively.

Table 2 Resonance frequency (f_0), return loss (S_{11}) at f_0, full band width at 3 dB above the minimum S_{11} at f_0 (f_{BW}), and quality factor (Q-factor)

Antenna	Resonance frequency, f_0 (MHz)	S_{11} at f_0 (dB)	f_{BW} (MHz)	Q-factor
SQ1	13.718	− 36.451	0.394	34.817
SQ2	13.193	− 30.983	0.445	29.647
SQ3	13.832	− 20.295	1.779	7.775
SP1	15.553	− 40.791	0.199	78.156
SP2	15.262	− 23.393	0.859	17.767
SP3	13.903	− 16.258	1.920	7.241

Acknowledgements

This work was supported by the US National Science Foundation under grant number OIA-1946231 and the Louisiana Board of Regents for the Louisiana Materials Design Alliance (LAMDA). The authors would like to thank the Nanofabrication facility at Louisiana State University and Dr. August Gallo from the Chemistry department at University of Louisiana at Lafayette.

Author contributions

JC: writing–original draft, validation, formal analysis, investigation, data curation, visualization. WW: validation, formal analysis, investigation, data curation, visualization. KY: investigation, data curation. SJ: writing–review & editing, conceptualization, methodology, resources, supervision, project administration, funding acquisition.

Funding

This work was supported by the US National Science Foundation under Grant Number OIA-1946231 and the Louisiana Board of Regents for the Louisiana Materials Design Alliance (LAMDA).

Data availability

The datasets generated during and/or analyzed during the current study are available from the corresponding author on reasonable request.

Declarations

Conflict of interest The authors have no relevant financial or non-financial interests to disclose.

References

1. R. Singh, E. Singh, H.S. Nalwa, Inkjet printed nanomaterial based flexible radio frequency identification (RFID) tag sensors for the internet of nano things. RSC Adv. **7**, 48597–48630 (2017)
2. S. Amendola, A. Palombi, G. Marrocco, Inkjet printing of epidermal RFID antennas by self-sintering conductive ink. IEEE Trans. Microw. Theory Tech. **66**, 1561–1569 (2018)
3. K. Fukuda, T. Someya, Recent progress in the development of printed thin-film transistors and circuits with high-resolution printing technology. Adv. Mater. **29**, 1602736 (2017)
4. S. Wang, J. Xu, W. Wang, G.-J.N. Wang, R. Rastak, F. Molina-Lopez, J.W. Chung, S. Niu, V.R. Feig, J. Lopez, T. Lei, S.-K. Kwon, Y. Kim, A.M. Foudeh, A. Ehrlich, A. Gasperini, Y. Yun, B. Murmann, J.B.H. Tok, Z. Bao, Skin electronics from scalable fabrication of an intrinsically stretchable transistor array. Nature **555**, 83–88 (2018)
5. Y. Zhang, N. Anderson, S. Bland, S. Nutt, G. Jursich, S. Joshi, All-printed strain sensors: building blocks of the aircraft structural health monitoring system. Sens. Actuators A **253**, 165–172 (2017)
6. B.W. An, J.H. Shin, S.-Y. Kim, J. Kim, S. Ji, J. Park, Y. Lee, J. Jang, Y.-G. Park, E. Cho, Smart sensor systems for wearable electronic devices. Polymers **9**, 303 (2017)
7. L. Mo, Z. Guo, L. Yang, Q. Zhang, Y. Fang, Z. Xin, Z. Chen, K. Hu, L. Han, L. Li, Silver nanoparticles based ink with moderate sintering in flexible and printed electronics. Int. J. Mol. Sci. **20**, 2124 (2019)
8. I.J. Fernandes, A.F. Aroche, A. Schuck, P. Lamberty, C.R. Peter, W. Hasenkamp, T.L.A.C. Rocha, Silver nanoparticle conductive inks: synthesis, characterization, and fabrication of inkjet-printed flexible electrodes. Sci. Rep. **10**, 8878 (2020)
9. L. Mo, Z. Guo, Z. Wang, L. Yang, Y. Fang, Z. Xin, X. Li, Y. Chen, M. Cao, Q. Zhang, L. Li, Nano-silver ink of high conductivity and low sintering temperature for paper electronics. Nanoscale Res. Lett. **14**, 197 (2019)
10. A. Kamyshny, S. Magdassi, Conductive nanomaterials for printed electronics. Small **10**, 3515–3535 (2014)
11. Z. Zhang, W. Zhu, Controllable synthesis and sintering of silver nanoparticles for inkjet-printed flexible electronics. J. Alloys Compd. **649**, 687–693 (2015)
12. S.V.K. Abhinav, V.K. Rao, R.P.S. Karthika, S.P. Singh, Copper conductive inks: synthesis and utilization in flexible electronics. RSC Adv. **5**, 63985–64030 (2015)
13. S. Magdassi, M. Grouchko, A. Kamyshny, Copper nanoparticles for printed electronics: routes towards achieving oxidation stability. Materials **3**, 4626–4638 (2010)
14. Z. Yu, F. Huang, T. Zhang, C. Tang, X. Cui, C. Yang, Effects of different thermal sintering temperatures on pattern resistivity of printed silver ink with multiple particle sizes. AIP Adv. **11**, 115116 (2021)
15. C.Y. Lai, C.F. Cheong, J.S. Mandeep, H.B. Abdullah, N. Amin, K.W. Lai, Synthesis and characterization of silver nanoparticles and silver inks: review on the past and recent

technology roadmaps. J. Mater. Eng. Perform. **23**, 3541–3550 (2014)
16. Y. Jo, S.J. Oh, S.S. Lee, Y.H. Seo, B.H. Ryu, J. Moon, Y. Choi, S. Jeong, Extremely flexible, printable ag conductive features on pet and paper substrates via continuous millisecond photonic sintering in a large area. J. Mater. Chem. C **2**, 9746–9753 (2014)
17. C.-F. Li, W. Li, H. Zhang, J. Jiu, Y. Yang, L. Li, Y. Gao, Z.-Q. Liu, K. Suganuma, Highly conductive Ag paste for recoverable wiring and reliable bonding used in stretchable electronics. ACS Appl. Mater. Interfaces **11**, 3231–3240 (2019)
18. S.K. Volkman, S. Yin, T. Bakhishev, K. Puntambekar, V. Subramanian, M.F. Toney, Mechanistic studies on sintering of silver nanoparticles. Chem. Mater. **23**, 4634–4640 (2011)
19. K.S. Bhat, R. Ahmad, Y. Wang, Y.-B. Hahn, Low-temperature sintering of highly conductive silver ink for flexible electronics. J. Mater. Chem. C **4**, 8522–8527 (2016)
20. P. Scherrer, Bestimmung der Grösse und der inneren Struktur von Kolloidteilchen mittels Röntgenstrahlen. Nachr. Ges. Wiss. Göttingen **26**, 98 (1918)
21. J.I. Langford, A.J.C. Wilson, Scherrer after sixty years: a survey and some new results in the determination of crystallite Size. J. Appl. Cryst. **11**, 102 (1978)
22. H. Maroma, M. Eizenberg, The effect of surface roughness on the resistivity increase in nanometric dimensions. J. Appl. Phys. **99**, 123705 (2006)
23. V. Timoshevskii, Y. Ke, H. Guo, D. Gall, The influence of surface roughness on electrical conductance of thin Cu films: an ab initio study. J. Appl. Phys. **103**, 113705 (2008)
24. P.Y. Zheng, T. Zhou, B.J. Engler, J.S. Chawla, R. Hull, D. Gall, Surface roughness dependence of the electrical resistivity of W(001) layers. J. Appl. Phys. **122**, 095304 (2017)
25. G. Palasantzas, Surface roughness and grain boundary scattering effects on the electrical conductivity of thin films. Phys. Rev. B **58**, 9685 (1998)
26. H. Bishara, S. Lee, T. Brink, M. Ghidelli, G. Dehm, Understanding grain boundary electrical resistivity in Cu: the effect of boundary structure. ACS Nano **15**, 16607–16615 (2021)
27. M. Ojeda, E. Iglesia, Formic acid dehydrogenation on au-based catalysts at near-ambient temperatures. Angew. Chem. Int. Ed. Engl. **48**, 4800 (2009)
28. N.J. Petch, The cleavage strength of polycrystals. J. Iron Steel Inst. **174**, 25–28 (1953)
29. S.N. Naik, S.M. Walley, The Hall-Petch and inverse Hall-Petch relations and the hardness of nanocrystalline metals. J. Mater. Sci. **55**, 2661–2681 (2020)
30. R.W. Armstrong, 60 years of Hall–Petch: past to present nanoscale connections. Mater. Trans. **55**, 2–12 (2014)
31. AN2972 Application note: how to design an antenna for dynamic NFC tags, STMicroelectronics, pp. 1–26 (2019). https://www.st.com/resource/en/application_note/cd00232630-how-to-design-an-antenna-for-dynamic-nfc-tagsstmicroelectronics.pdf
32. AN2866 Application note: how to design a 13.56 MHz customized antenna for ST25 NFC/RFID tags, pp. 1–20 2021.
33. X. Niu, H. Zhang, Design and simulation of 13.56 MHz RFID reader antenna, in *Proceedings of ICCT*. (2015), pp.400–402
34. H. Lehpamer, *RFID design principles*, 2nd edn. (Artech House, Norwood, 2012), pp.150–152
35. A.H. Sarhadi, A. Hashemi, H. Emami, Optimization of Q factor in complementary spiral resonator for RFID application, in *21st telecommunications forum TELFOR 2013, Serbia, Belgrade, Nov. 26–28*. (2013), pp. 26–28. https://doi.org/10.1109/TELFOR.2013.6716323
36. J.J. Baek, S.W. Kim, K.H. Park, M.J. Jeong, Y.T. Kim, Design and performance evaluation of 13.56-MHz passive RFID for e-skin sensor application. IEEE Microw. Wirel. Compon. Lett. **28**, 1074–1076 (2018)
37. T. Athauda, N.C. Karmakar, The realization of chipless RFID resonator for multiple physical parameter sensing. IEEE Internet Things J. **6**, 5387–5396 (2019)
38. D.A. Feld, R. Parker, R. Ruby, P. Bradley, S. Dong, After 60 years: a new formula for computing quality factor is warranted, in *2008 IEEE ultrasonics symposium, Beijing, China, Nov. 2–5*. (2008), pp.2–5
39. X. Niu, H. Zhang, Design and simulation of 13.56 MHz RFID reader antenna, in *2015 IEEE 16th International Conference on Communication Technology (ICCT), Hangzhou, China*. (2015), pp.400–402